INTERFACE CONDITIONS OF FINITE-DIFFERENCE COMPACT SCHEMES FOR COMPUTATIONAL AEROACOUSTICS

Tomoaki Ikeda, Takahiro Sumi, Takuji Kurotaki
Japan Aerospace Exploration Agency

Keywords: *Compact scheme, Computational aeroacoustics, Characteristics condition*

Abstract

Computational aeroacoustics has been widely applied as high-performance computer systems have been available, as well as highly accurate numerical algorithms developed to directly resolve acoustical disturbance. An interface treatment to connect two or more grid boundaries provides flexibility to handle complex geometries, such as a high-lift device or turbine cascade, on a generalized coordinate system; one of common examples is a multi-block approach. When used with a compact scheme, however, its accuracy and stability may be degraded seriously by the boundary treatment that arises at a block interface. This paper discusses how to construct characteristic-based interface conditions, especially suited to computational aeroacoustics, for the use with a finite-difference compact scheme. The validity of current development is demonstrated through simple convection test cases, as well as an application problem of computational aeroacoustics.

1 Introduction

Compact finite-difference schemes are now commonly utilized to achieve higher accuracy in many fields of computational analysis. Their low-dispersion nature is favored especially in the direct numerical simulations (DNS) or large-eddy simulations (LES) of turbulent flows, as well as aeroacoustics, to resolve short wavelengths with high accuracy. One of the advantages of finite-difference schemes is that their formulations can be extended easily to general coordinates. Recently, many application studies have been done on generalized curved grids using upwind or centered compact schemes. Also, the attempts to solve more complicated geometries are being made through multi-block approaches [2, 14]. Usually, in a multi-block framework, the numerical grids must be carefully constructed to smoothly bridge grid topologies at a block connection, since the abrupt variation lowers the accuracy of flow simulations. With increasing geometrical complexity, however, it would be inhibitive to meet this requirement. On the other hand, Kim and Lee [8] introduced the characteristic interface conditions that do not necessarily require the smooth connection at a block interface, where the characteristic relations are applied from both sides; this approach has been extended to a more general treatment that alleviates the local-axis dependence across an interface [13]. However, it is still unclear how these treatments affect the accuracy of compact schemes, especially when used in computational aeroacoustics (CAA).

One of the difficulties in interface conditions is the boundary treatment of compact schemes at the interface. Since the derivatives are expressed implicitly in compact schemes, even if formally high-order schemes are used for inner nodes, actual accuracy may degrade seriously, or even result in unstable modes by using inappropriate approximations. Many studies have been

conducted for this issue. For instance, Carpenter et al. [1] performed the semi-discrete eigenvalue analysis, originally developed by Strikwerda [11], on high-order boundary schemes, and showed that increasing the accuracy of boundary conditions would lead to instability. From the view point of the Fourier analysis, Sengupta et al. [10] pointed out that the boundary implementation can be critical to the stability of compact schemes, by also applying the von-Neumann analysis, and derived a family of optimized upwind compact schemes. Also, to achieve more accurate schemes, optimization techniques were introduced to boundary closures [5, 6], combined with centered compact schemes.

In this paper, our aim is to construct a proper formulation of characteristic-based interface conditions for the use with compact schemes. Here, we primarily concern the implementation of centered finite-difference compact schemes, which is suited to aeroacoustic problems on, for example, a low-Mach number flow, as well as turbulent flow. To develop a proper interface condition, the boundary closure of compact schemes will be first discussed using a Fourier mode analysis, and tested through one-dimensional convection problems. Next, the extension to multi-dimensions will be proposed and applied to a vortex convection on the grid with singularity. Finally, the developed interface condition is applied to a CAA test case, 2D flow past an airfoil, and a generated sound wave is quantitatively examined and discussed.

2 Analysis of the one-dimensional boundary closure

2.1 Modified wave-number analysis

To evaluate the accuracy of finite-difference schemes on phase space, it is common to utilize a Fourier mode analysis. When applying it to a compact scheme, however, the modified wave number of the scheme is not only a function of each mode, but also coupled spatially. A modified wave number is given as a form of implicit representation in an analytical expression; otherwise, in general, it must be solved with the dependence on the same modes at all other nodes, as shown in [5, 10].

Here we analyze a compact scheme applied to a convection problem for a function $u(x,t)$ defined over a bounded domain $x \in [0,L]$ at $t > 0$. After the homogeneous discretization of the domain by N nodes, or $N-1$ cells, the spatial derivative u' can be approximated by an implicit form:

$$\sum_{l=j-n_L}^{j+n_R} a_{j,l} u'_l = \frac{1}{h} \sum_{l=j-m_L}^{j+m_R} b_{j,l} u_l, \qquad (1)$$

for $j = 1,2,\ldots,N$, where n_L, n_R, m_L, and m_R represent the number of nodes required for the given stencils; h is the width of a cell; $a_{j,l} = 1$ if $j = l$. For inner nodes, we usually apply uniform coefficients, namely, $a_{i,i+m} = a_{j,j+m}$ and $b_{i,i+m} = b_{j,j+m}$ for $i \neq j$. However, since the domain is bounded, we need to shift the stencils, and therefore modify the coefficients near boundaries; this modification on a compact scheme is often referred as boundary compact scheme. Consequently, this also alters the behavior of modified wave numbers at all the locations. Since the spatial derivatives of a boundary scheme are usually coupled as those for inner nodes, its modified wave numbers are also coupled as a system of equations.

By applying discrete Fourier expansion, u_j can be written as

$$u_j = \sum_n \hat{u}_n \mathrm{e}^{\mathrm{i}k_n h j}, \qquad (2)$$

where $\hat{u}_n$ is a Fourier coefficient of the n-th mode, $k_n = 2\pi n/L$, and the summation on n is taken for a suitable range of N modes, e.g., $-N/2$ to $N/2-1$ for an even number of N. Then, by definition, the Fourier coefficient of the approximated derivative term can be expressed by using the corresponding modified wave number $\kappa_n^{(j)}$ defined for the node j, as $\mathrm{i}\kappa_n^{(j)}\hat{u}_n$. By substituting this and Eq. (2) into Eq. (1), we obtain an implicit representation of modified wave numbers for the n-th Fourier mode,

$$\sum_l a_{j,l} \mathrm{i}\kappa_n^{(l)} \mathrm{e}^{\mathrm{i}k_n h(l-j)} = \frac{1}{h} \sum_m b_{j,m} \mathrm{e}^{\mathrm{i}k_n h(m-j)}. \qquad (3)$$

This can be solved using a conventional multi-diagonal matrix inversion technique. However, since all the modified wave numbers are coupled, it would not be straight forward to derive effective coefficients for a boundary compact scheme, unlike the optimization for inner nodes by reducing a phase error [e.g., 9]. As was also pointed out in [5], the optimized sets of boundary schemes in [6, 8] were constructed without taking the above coupling into account. Therefore, their optimized schemes show a considerable phase error near the boundary node, as shown in Fig. 1. On the other hand, in [5], optimized boundary schemes were obtained by calibrating free parameters included only in the boundary-node scheme to minimize phase error, while standard Padé schemes were used for inner nodes.

2.2 Test 1D problem

As a test case of characteristic interface conditions, we consider one-dimensional linear wave equation with convection velocity c (>0), imposing the periodic boundary condition. A one-dimensional periodic problem may be solved simply by using an interior scheme with a common periodic inversion technique. However, since our objective is to examine the effect of boundary schemes, the periodicity here is enforced by a characteristic boundary condition applied to bounded schemes. Namely, we impose the continuity of the spatial derivative at both ends of domain as,

$$\frac{\partial u}{\partial t}+c\frac{\partial u}{\partial x}=0, \quad \left.\frac{\partial u}{\partial x}\right|_{x=0}=\left.\frac{\partial u}{\partial x}\right|_{x=L}. \qquad (4)$$

Since the convection velocity is positive, the derivative at $x=0$ should be determined by that evaluated at $x=L$. Then, a bounded compact scheme given in Eq. (1) can be applied to this test case.

The above boundary implementation is one simple application of characteristic interface conditions for a one-dimensional scalar problem. For example, we could place the discontinuity of grid spacing across the periodic boundary by using a non-uniform grid, stretched gradually. Also in multi-dimensions, the characteristic interface condition to enforce periodicity may be effective because the requirement of grid smoothness across the periodic boundary can be removed, as proposed in [8]. However, although we employ uniform grid spacing in this one-dimensional test, we would clarify the adverse effects caused by the characteristic interface condition combined with the use of bounded schemes.

In [8], the interface condition may reduce to one-dimension, originally developed for a three-dimensional case, as follows:

A-1 The spatial derivative is evaluated by an optimized bounded compact scheme that uses a centered difference for inner nodes, and a one-sided compact stencil at boundary nodes, without specifying any boundary conditions.

A-2 Afterwards, the boundary condition is imposed: the derivative at $x=0$ is replaced by that evaluated at $x=L$.

As observed in Fig. 1, since the convective velocity c is positive, the positive $\mathrm{Im}(\kappa)$ acts as *anti*-diffusion at relatively large k. This is primarily due to the downwind or downwind-biased differences employed on these nodes. By enforcing the above characteristics-based treatment, we also regain upwinding diffusion for an interface. Nevertheless, usually on large wavenumbers, it is more desirable to impose positive diffusion also to near-boundary nodes.

Besides, as seen in [5], the boundary node is apt to exhibit a relatively large phase error if its scheme is evaluated with a one-sided compact difference, i.e., $a_{j,l}\neq 0$ for $j\neq l$ where $j=1$ or N, in Eq. (1). The optimization process proposed in [5] showed a difficulty in reducing a phase error at the boundary node as well. The degradation of accuracy at boundary nodes may not be so crucial to a simple non-periodic boundary applied to a linear convection problem. However, when employed with characteristic interface or boundary conditions, especially in a multi-dimensional problem, e.g., a vortex convected along an in-

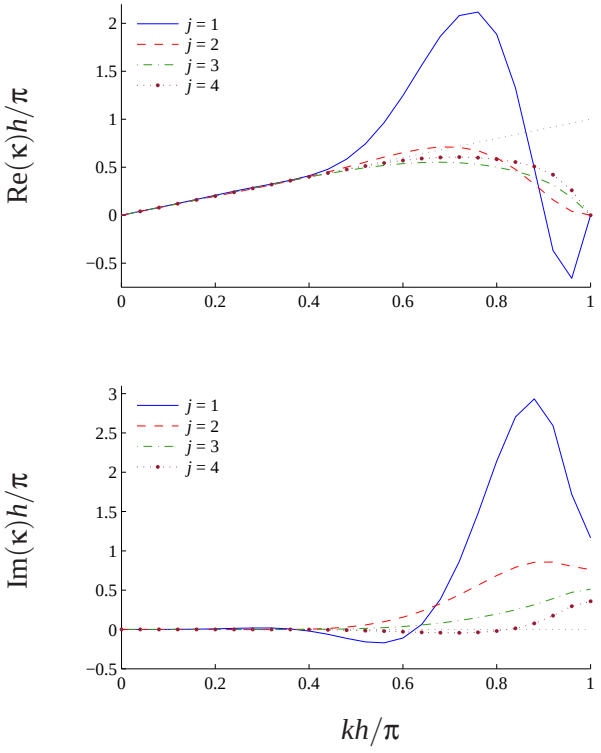

Fig. 1 Modified wave numbers for the scheme given in [8] near the left boundary. Total number of nodes N is 51. $\mathrm{Re}(\kappa)$ and $\mathrm{Im}(\kappa)$ denote the real and imaginary parts of a modified wave number, respectively.

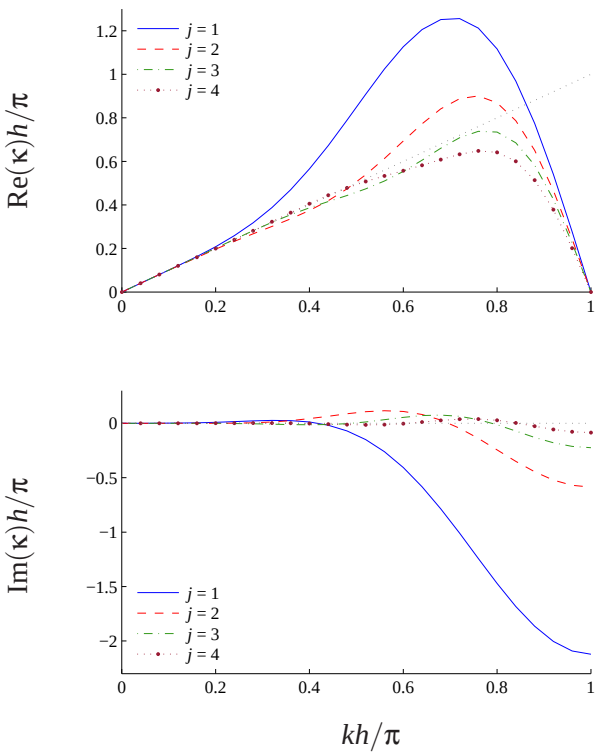

Fig. 2 Modified wave numbers for the present proposed scheme near the left boundary. Total number of nodes N is 51.

terface connection, or acoustic disturbances reflected back and forth between two solid walls, an inferior boundary scheme could cause an unphysical disturbance from its boundary or interface.

In order to remove this difficulty, explicit stencils are used in [10] for the boundary and near-boundary nodes: second-order one-sided difference for the boundary node, and an optimized third-order difference for its adjacent node. Coupled with optimized upwind compact schemes, they attained stable implementations in terms of both modified wave numbers and von Neumann analysis.

By using an explicit scheme for the boundary node coupled with centered compact schemes, we can make a modification on the implementation of characteristic interface conditions as follows:

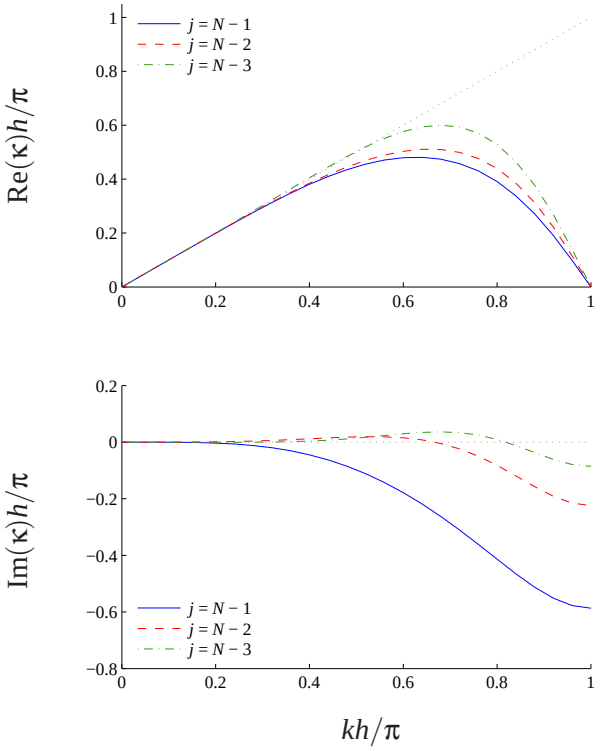

Fig. 3 Modified wave numbers for the present proposed scheme near the right boundary.

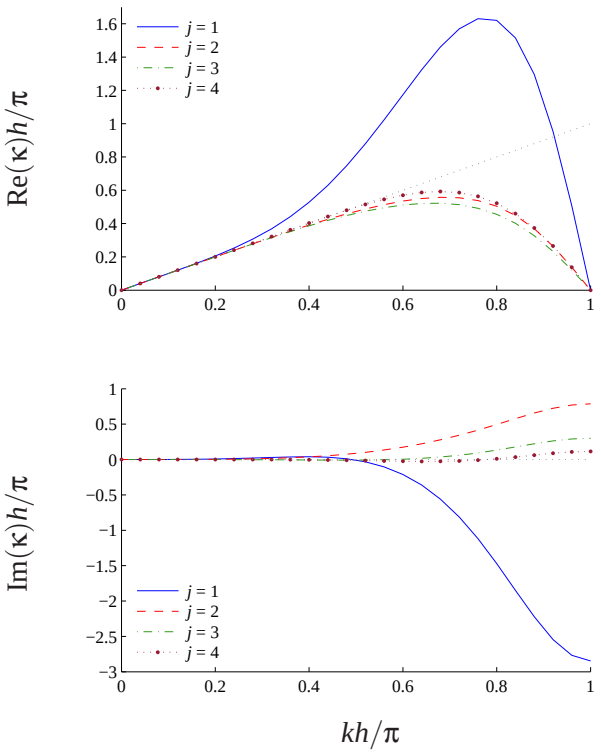

Fig. 4 Modified wave numbers for SC scheme near the left boundary.

B-1 Evaluate the derivative at the upwind-side boundary node, $x = L$ in Eq. (4), by using an explicit one-sided difference scheme.

B-1 Employ the above as the boundary conditions, u'_1 and u'_N; then, solve the system of equations of a compact scheme for the derivatives at inner nodes.

Here, we propose one test scheme to carry out the above implementation. For the boundary node $j = N$, the standard third-order difference is adopted as follows:

$$u'_j = \frac{1}{6h}\left(11u_j - 18u_{j-1} + 9u_{j-2} - 2u_{j-3}\right). \quad (5)$$

On the other hand, for the inner nodes, the standard Padé scheme is employed: the fourth-order centered difference for the nodes adjacent to boundaries, and the sixth-order difference elsewhere. In the following, the scheme defined here is called *present* scheme. The modified wave numbers near the left boundary, $j = 1$, are obtained as in Fig. 2, while those near the right boundary are shown in Fig. 3. Although anti-diffusion still arises in the middle to relatively large wavenumbers, the scheme has shifted toward a more stable side by imposing the characteristic relation as the boundary conditions of the present compact scheme. The resolution in the phase space is relatively low, as expected from the formulation of the present scheme, since standard schemes are employed with no optimization technique.

For comparison, we also test the compact representation for boundary nodes. The standard third-order one-sided compact difference is used instead of the above explicit scheme, which is defined as ($j = N$):

$$u'_j + 2u'_{j-1} = \frac{1}{2h}\left(5u_j - 4u_{j-1} - u_{j-2}\right). \quad (6)$$

For the inner nodes, however, the same Padé scheme is employed as the present scheme. This combination of compact differences is used in other literatures [e.g., 12], and also examined in [5]. The original interface implementation [8] is applied to this standard compact scheme, which is called *SC* scheme here. The modified wave number distributions are shown in Fig. 4. Although the characteristic condition is imposed at $j = 1$, it does not affect the phase behavior of other near-boundary nodes, which shows anti-diffusion in large k. Also as the family of compact representations for the boundary scheme, the scheme given in [8] is referred as *KL* scheme, while the optimized scheme derived by [5] is defined as *J* scheme in the following.

2.3 Linear convection test

Here, four different schemes that use centered compact differences for inner nodes are examined using the linear convection problem, Eq. (4). In addition, an optimized upwind compact scheme, OUCS-2 defined in [10] is also compared as a reference case: here, it is referred as *OU* scheme. As an initial condition, a periodic distribution is given as the form:

$$u_o = \cos\left(\frac{2m\pi x}{L}\right)\exp\left[-C\left(x - \frac{L}{2}\right)^2\right]. \quad (7)$$

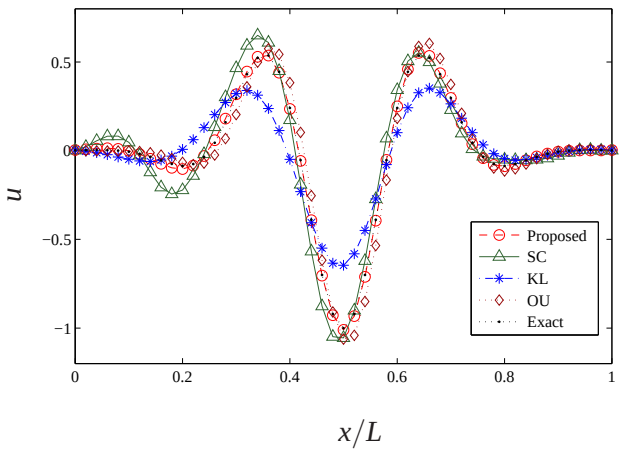

Fig. 5 One-dimensional test case after the run period of $20L/c$: $m = 3$ in Eq. (7).

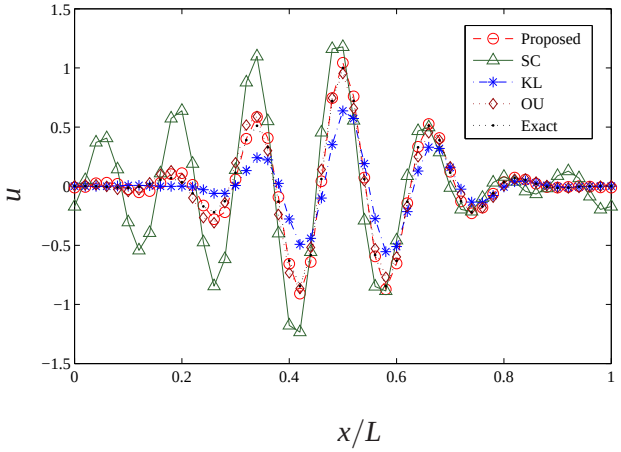

Fig. 6 One-dimensional test case after the run period of $5L/c$: $m = 6$ in Eq. (7).

In this test, $C = 25$, and $m = 3$ and 6 are employed. The total number of nodes N is 51, and the Courant-Friedrichs-Lewy (CFL) number is chosen to be 0.2. Each scheme is advanced using the standard fourth-order Runge-Kutta scheme.

Figs. 5 and 6 show the results after the run period of $20L/c$ and $5L/c$, respectively, for $m = 3$ and 6. In both cases, the J scheme given in [5] quickly diverged, and therefore not shown; the stability of the J scheme will be discussed in a few more details in Section 2.4 by using an eigenvalue analysis. The KL scheme shows a considerable numerical diffusion, which can be predicted by the modified wave number distribution, Fig. 1. The boundary nodes have a fairly large dissipative error, which may add stability against the anti-diffusion produced at near-boundary nodes. On the other hand, the SC scheme induced a spurious high-frequency noise added on the initial shape, which is specifically dominant in Fig. 6: the solution gradually tends to diverge as an additional time integration due to this short-wavelength error. Supposedly, u'_1 evaluated in Eq. (1) by the downwind difference caused this instability through the implicit coupling of the compact scheme.

The present scheme of an interface implementation, however, agrees well with the exact solution, while the OU scheme also shows a reasonably accurate prediction with only a slight deviation seen in Fig. 5, probably due to its lower-order boundary schemes. Both the schemes use non-compact, explicit differences, which prefix a boundary condition of compact differences, at boundary nodes. These observations indicate that the improper implementation of a boundary condition for compact schemes not only affects the stability, but can significantly lower the accuracy, which is critical to attain an accurate interface condition.

2.4 Semi-discrete eigenvalue analysis

This section briefly summarizes a stability criterion of linear convection, $\partial_t u + \partial_x u = 0$, using the eigenvalues of a semi-discrete system, namely the G-K-S stability analysis [e.g., 1, 9, 11]. Here we assume that the function $u(x,t)$ is discretized spatially with a uniform grid in $x \in [0,L]$, but still continuous in time. We apply a compact scheme to the spatial derivative as:

$$A\boldsymbol{u}' = \frac{1}{h}B\boldsymbol{u}, \tag{8}$$

where $\boldsymbol{u} = [u_i]$, $A = [a_{i,j}]$, and $B = [b_{i,j}]$ in Eq. (1). Then, its stability can be estimated through an eigenvalue problem,

$$\lambda A\boldsymbol{u} = -B\boldsymbol{u}. \tag{9}$$

To fulfill a stability criterion, the real part of λ must be zero or negative.

In fact, the distribution of eigenvalues λ may be affected greatly by the implementation of boundary conditions. Since no boundary condition is needed at the outlet $x = L$ ($j = N$), we only require an inlet boundary condition, $x = 0$ ($j = 1$). Here, we specify the spatial derivative u' at $j = 1$ as the boundary condition, instead of fixing $u(0,t) = u_1(t)$. When solving Eq. (8) for $\boldsymbol{u}'$, however, we assume that its right-hand side, $\boldsymbol{u}$ is given, including u_1. We consider the following three types of boundary conditions:

BC-1 Explicitly prescribe u'_1 when solving Eq. (8).

BC-2 Provide no boundary condition when solving Eq. (8). Afterwards, replace u'_1 by the prescribed value.

BC-3 Impose the periodic boundary condition by a characteristic relation, $u'_1 = u'_N$, as tested in the previous section.

BC-2 corresponds to the characteristic boundary conditions suggested by [7]. Also in [1], a stability analysis was performed based on the inflow boundary condition essentially equivalent to BC-2, while BC-1 was used in [9] in the eigenvalue analysis, as u'_1 set to zero. The implementation of a periodic boundary condition, BC-3, differs depending on whether the boundary nodes employ a compact difference or not, as done in Section 2.3.

In Fig. 7, the above three boundary conditions are compared by using the J scheme [5]. The diagram shows two distinct unstable eigenvalues in the right half of the plane for BC-2 and 3, although the scheme is stable for BC-1. The reason of the diverged solution by the J scheme in the linear convection test of Eq. (4) can be attributed to these unstable modes.

In Figs. 8 and 9, two additional sets that use the standard Padé schemes are compared: the present scheme and SC scheme. By using BC-1 and 2, these two schemes show very similar distributions. Although the eigenvalues of BC-1 are shifted toward a more stable region as also observed in Fig. 7, both boundary conditions are stable. However, both the schemes hold

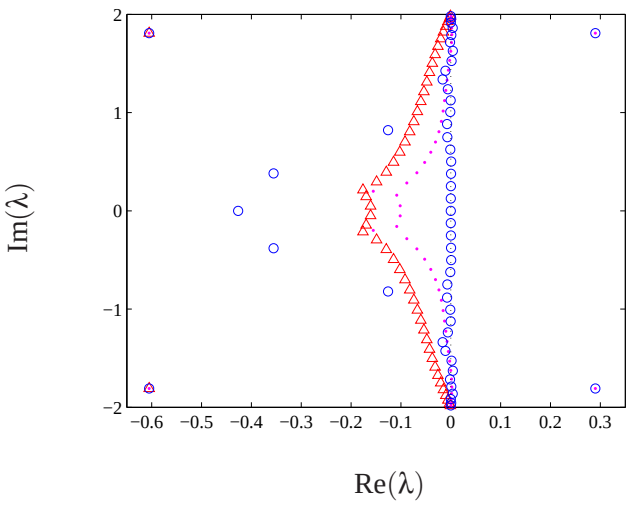

Fig. 7 Distributions of eigenvalues obtained by the J scheme, for three boundary conditions: △, BC-1; ·, BC-2; ○, BC-3. Total number of nodes N is 51.

positive-real eigenvalues on the condition BC-3. By imposing a characteristic-based periodic boundary condition, there exist several diffusive eigenvalues in the left half of the complex plane. Although those negative-real eigenvalues of the present scheme are located in a more stable region than those of the SC scheme, the rest of the eigenvalues are aligned closely to the imaginary axis in both the schemes; in fact, some of them lie in the right half of the plane. This is the consequence due to the enforcement of a periodic boundary condition, which indicates an infinite-time integration using bounded schemes. If the linear convection test carried out in Section 2.3 is run for a considerably long period of time, these unstable modes may become apparent, although the SC scheme showed an amplification of short waves in Fig. 6 within less iterations.

As will be seen in Section 4.1, the difference in the implementation of boundary schemes severely affects the accuracy in an aeroacoustic problem even without periodic boundary conditions. In practice, to avoid the instability associated with high-frequency errors, if any exists, the use of explicit low-pass filters may be effective with a centered compact scheme.

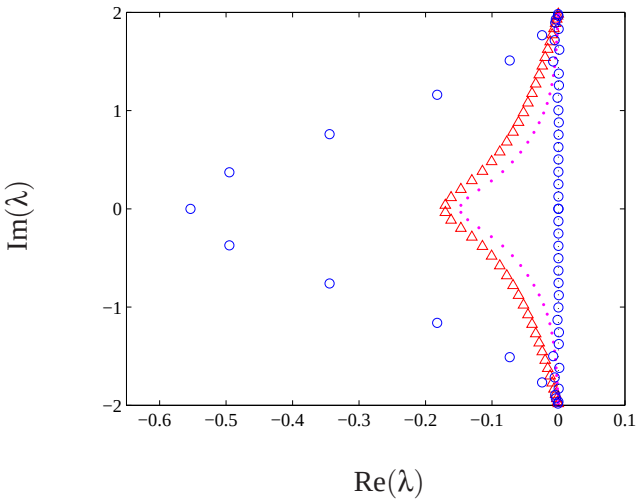

Fig. 8 Distributions of eigenvalues obtained by the present scheme. See the caption in Fig. 7.

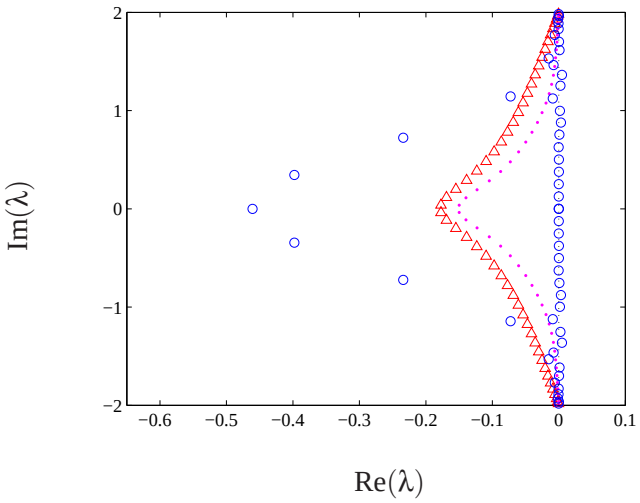

Fig. 9 Distributions of eigenvalues obtained by the SC scheme. See the caption in Fig. 7.

3 Formulation in multi-dimensions

The compact schemes whose boundary nodes utilize one-sided compact differences can be applied directly to a multi-dimensional problem in conjunction with the characteristic interface condition. After all the convection terms are computed by a compact scheme, their boundary values are updated through a quasi-linear one-dimensional characteristic relation, which can be written as:

$$\frac{\partial \boldsymbol{R}}{\partial t} + \bar{\lambda}\frac{\partial \boldsymbol{R}}{\partial \xi} = \bar{P}^{-1}\boldsymbol{S}_\xi, \tag{10}$$

where $\boldsymbol{R}$ represents the characteristic differential variables; $\bar{\lambda}$ is the diagonal matrix of the speeds of characteristics; $\bar{P}^{-1}$ is the transformation matrix for characteristic decomposition; $\boldsymbol{S}_\xi$ denotes the reduced source term, including the convection terms except the ξ-direction, as well as the viscous terms. For simplicity, we only consider a two-dimensional case, and assume the ξ-axis is the direction normal to the interface in computational coordinates. These assumptions are not requirements; we can easily extend the following discussion to a general three-dimensional problem. The decomposed convection term in the ξ-direction is derived by multiplying $\bar{P}^{-1}$ from the left to:

$$\begin{aligned}\boldsymbol{C}_\xi &\equiv J\left[\frac{\partial \hat{\boldsymbol{E}}}{\partial \xi} - \left\{\boldsymbol{E}\frac{\partial}{\partial \xi}\left(\frac{\xi_x}{J}\right) + \boldsymbol{F}\frac{\partial}{\partial \xi}\left(\frac{\xi_y}{J}\right)\right\}\right] \\ &= \xi_x\frac{\partial \boldsymbol{E}}{\partial \xi} + \xi_y\frac{\partial \boldsymbol{F}}{\partial \xi},\end{aligned} \tag{11}$$

so that $\bar{P}^{-1}\boldsymbol{C}_\xi = \bar{\lambda}\partial\boldsymbol{R}/\partial\xi$, where J is the transformation Jacobian; $\boldsymbol{E}$ and $\boldsymbol{F}$ are the inviscid fluxes in the x- and y-directions, respectively; $\hat{\boldsymbol{E}} = (\xi_x\boldsymbol{E} + \xi_y\boldsymbol{F})/J$ is the transformed flux in the ξ-direction.

However, when applying Eq. (10) to the present scheme to determine the boundary condition, the source term $\boldsymbol{S}_\xi$ must be precomputed carefully, since the convection terms that arise in $\boldsymbol{S}_\xi$ are generally unknown at this stage before solving a compact scheme. In the following, we would introduce an alternative treatment for multi-dimensions as an extension of the characteristic-based interface condition, without directly utilizing the characteristic relation Eq. (10). Rather, a proper coordinate transformation is employed across an interface. A schematic of the general interface connection of two-dimensional grids is shown in Fig. 10.

When we would evaluate a ξ-derivative on the grid R as a characteristic entering from the opposite side, grid L, the spatial derivatives should

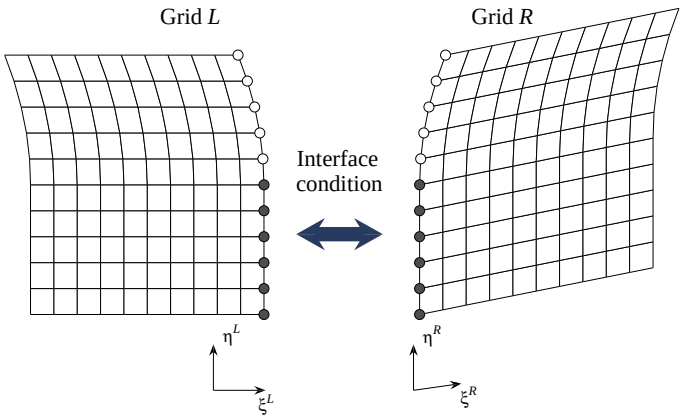

Fig. 10 A schematic of two grids, L and R, connected through an interface condition, applied to the nodes marked by black circles. White circles indicate any other boundaries, e.g., impermeable wall boundary.

be estimated using the information on the grid L. This can be achieved via the following coordinate transformation from the grid R to L:

$$\begin{aligned}\frac{\partial}{\partial \xi^R} &= x_{\xi^R}\frac{\partial}{\partial x} + y_{\xi^R}\frac{\partial}{\partial y}\\ &= x_{\xi^R}\left(\xi^L_x\frac{\partial}{\partial \xi^L} + \eta^L_x\frac{\partial}{\partial \eta^L}\right)\\ &\quad + y_{\xi^R}\left(\xi^L_y\frac{\partial}{\partial \xi^L} + \eta^L_y\frac{\partial}{\partial \eta^L}\right)\\ &= \left(\boldsymbol{d}_{\xi^R}\cdot\nabla\xi^L\right)\frac{\partial}{\partial \xi^L} + \left(\boldsymbol{d}_{\xi^R}\cdot\nabla\eta^L\right)\frac{\partial}{\partial \eta^L},\end{aligned} \tag{12}$$

where $\boldsymbol{d}_\xi = (x_\xi, y_\xi)$. The right-hand side of Eq. (12) can be understood as the directional derivative in the ξ^R-direction evaluated on the grid L. The second term, the derivative in the tangential direction η^L, represents the discrepancy of the direction of ξ-axis across an interface. The inner product $\boldsymbol{d}_{\xi^R}\cdot\nabla\eta^L$ will be sufficiently small if two grids are connected smoothly. In a finite-difference form, the first term $\partial/\partial\xi^L$ is evaluated by the one-sided difference shown in Eq. (5), whereas the second term $\partial/\partial\eta^L$ can be any high-order differences. In the following study, this tangential direction is evaluated by the same symmetric Padé scheme those used for inner nodes.

The implementation procedure of the proposed interface condition for a two-dimensional case can be summarized as follows:

1. On the boundary node of the grid R, compute the convection term in the ξ^R-direction evaluated on its-own grid, $\boldsymbol{C}_{\xi^R}\big|_R$ as shown in Eq. (11).
2. Likewise, evaluate $\boldsymbol{C}_{\xi^R}$ on the opposite side, grid L, by applying the transformation shown in Eq. (12), denoted $\boldsymbol{C}_{\xi^R}\big|_L$.
3. Apply characteristic decomposition to both $\boldsymbol{C}_{\xi^R}\big|_R$ and $\boldsymbol{C}_{\xi^R}\big|_L$, and retain only the components of upwind side for each convection velocity. Combine them to reform $\boldsymbol{C}^*_{\xi^R}$. Then, reassess the convection term in the ξ^R-direction through,

$$\begin{aligned}\frac{\partial \hat{\boldsymbol{E}}^*}{\partial \xi^R} &\equiv \frac{1}{J}\boldsymbol{C}^*_{\xi^R}\\ &\quad + \left\{\boldsymbol{E}\frac{\partial}{\partial \xi^R}\left(\frac{\xi^R_x}{J}\right) + \boldsymbol{F}\frac{\partial}{\partial \xi^R}\left(\frac{\xi^R_y}{J}\right)\right\}.\end{aligned} \tag{13}$$

4. On the boundary node of the grid L, follow the same process for $\boldsymbol{C}_{\xi^L}$.
5. Solve a compact scheme by using the resultant convection term for each grid as a boundary condition.

By taking these steps, since each side of the interface is evaluated in different numerical procedures, the physical variables will differ computed on each side. To ensure the continuity at the interface, they must be averaged in some way; here, we employ a simple arithmetic average.

We would note that the characteristic interface condition by [8] required the alignment of the gradient vectors of the coordinate normal to the interface; namely, $\nabla\xi^L \parallel \nabla\xi^R$ at the interface. However, the approach presented here does not. Geometrically, $\nabla\xi^R$ represents a vector normal to the surface of a constant ξ. Therefore, their requirement is naturally satisfied when both entire

boundary surfaces completely coincide. However, this does not hold on the interface shown in Fig. 10, as only a part of the surfaces are connected, if the metrics are evaluated by using a compact scheme, too. In generalized coordinates, metrics should be computed by the same compact scheme as that used in flow simulations [15]. If a part of one surface does not have a geometric correspondence with the other, where the interface conditions are meant to be excluded (e.g., the nodes marked by white circles in Fig. 10), the metrics evaluated there affect those at the interface connection, because a compact scheme has a global influence. Eventually the coordinate-gradient vectors of metrics do not have a common direction, even if the local grid topologies are identical. The present method can be extended to this type of grids; an application of this feature to a C-grid topology will be shown in Section 4.2.

On the other hand, if two interface surfaces correspond completely, the original formulation of characteristic interface conditions is still applicable. In stead of using the coordinate transformation shown in Eq. (12), $\boldsymbol{C}_{\xi R}$ evaluated on the grid L can be expressed as:

$$\boldsymbol{C}_{\xi R}\big|_L = \boldsymbol{C}_{\xi L}\big|_L - \boldsymbol{S}_{\xi L} + \boldsymbol{S}_{\xi R}, \qquad (14)$$

derived through the characteristic relation across the interface. In the original formulation, $\boldsymbol{S}_\xi$ contains the viscous terms, as well as the convection terms in the other directions. Since $\boldsymbol{C}_{\xi R}$ is sought as the boundary condition of the convection term, we may exclude the viscous terms from $\boldsymbol{S}_\xi$; nevertheless, they also cancel out in an analytical form. In this case, we can show that Eq. (14) is analytically equivalent to the application of the coordinate transformation, Eq. (12), to $\boldsymbol{C}_{\xi R}$. Therefore, the method developed here reduces to an alternative formulation of the characteristic interface condition.

4 Test cases

In this section, two non-linear tests are presented, solved in two-dimensions. In each case, interface conditions are applied to the connection of the grid lines bent abruptly. The fluid property is assumed to be of air; the specific-heat ratio is treated to be constant, 1.4. For the time advancement of each scheme, the standard fourth-order Runge-Kutta scheme is used.

4.1 Vortex convection across an interface

Here, a vortex is convected with an inviscid uniform flow, whose Mach number is 0.5. The following swirl velocity V_θ and associated pressure distribution is provided as an initial condition:

$$V_\theta \equiv \varepsilon U_\infty \frac{r}{R}\exp\left(-\frac{r^2}{2R^2}\right),$$
$$p' \equiv p - p_\infty = -\frac{1}{2}\rho\varepsilon^2 U_\infty^2 \exp\left(-\frac{r^2}{R^2}\right),$$

where U_∞ and p_∞ are the velocity and pressure of the inflow, respectively; r is the distance from the vortex center at the initial state; R and ε are the parameters that determine the vortex size and strength. Here, $R = 0.2$ and $\varepsilon = 5\times10^{-3}$, at which the maximum of V_θ corresponds to 0.3% of U_∞. Also, the maximum pressure deviation from p_∞ is about $4.5\times10^{-6}p_\infty$; this pressure level is affected easily by the numerical scheme of low accuracy. In the following description, U_∞ is assumed to be 1.0.

Fig. 11 shows the grid used in this test, and also the initial pressure distribution presented in an overhead view. The grid is bent abruptly by 30° at $x = 0$, where the interface conditions are applied; the employed resolution is 120×120 for the given field. If this bent grid is treated continuously with no interface condition applied, the vortex will be smeared substantially by high-frequency errors, which induces a considerable level of fictitious noise. At $t = 0$, the vortex center is placed at $(x,y) = (-1,0)$, and conveyed in the x-direction with the flow. The simulation is run at $\Delta t = 5.0\times10^{-3}$ that corresponds to CFL $= 0.46$. The vortex center reaches the grid interface at $t = 1.0$.

In this test, we examine two different boundary implementations for a compact scheme: one is the SC scheme defined in Section 2.2, which uses a third order compact scheme for boundary nodes, and the other is the test scheme proposed

in the present paper. As seen in the linear convection test, the implementation procedure of boundary conditions is more crucial for stability. Therefore, only these two schemes are compared by employing the standard Padé schemes for inner nodes. No additive artificial diffusion or filtering technique is applied to the schemes; the characteristics of the original formulations are of interest in this test. To outer boundaries, the characteristic inflow and outflow conditions given in [7] are used. However, the modification used with an explicit difference is also implemented in the present scheme; namely, BC-1 is employed as defined in Section 2.4, while the SC scheme uses the implementation equivalent to BC-2.

Figs. 12 and 13 compare the temporal variation of pressure distributions for the two schemes, when and after the vortex crosses the grid interface. In this simulation, the pressure field is rather sensitive than the velocity field. The difference in the velocity, or vorticity fields, is almost indiscernible; they are not shown here. However, the presented pressure fields clearly exhibit the effects of numerical treatments. In Fig. 12, the original bell shape is distorted across the interface at $t = 1.0$ by using the SC scheme. Away from the interface, the vortex regains its original pressure shape. However, as the vortex passes by, a relatively low-frequency noise that resembles a sound wave is emitted from the interface toward upstream. Besides, sharp peaks can be recognized at the inflow boundary at $t = 1.5$. They are not the wave propagation from the interface, since not enough time has passed from $t = 1.0$. Rather, they would be the indication of the numerical instability held by the boundary implementation. On the other hand, as seen in Fig. 13, the present scheme significantly improves the conservation of the original pressure shape. Although still recognizable, the spurious noises are suppressed successfully; they are within 6% of the maximum of $|p'|$ during this run, while the maximum error of the SC scheme reaches nearly 40%, due to the distorted vortex profile at $t = 1.0$.

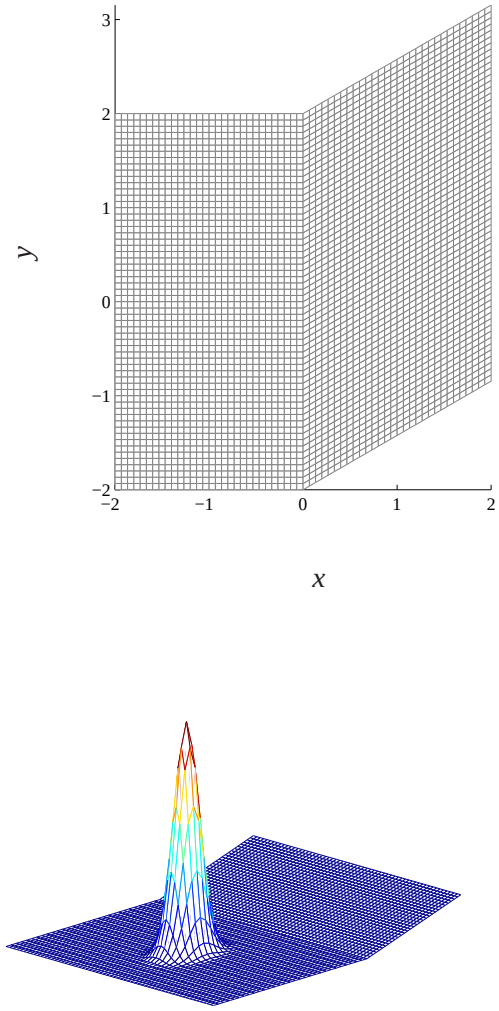

Fig. 11 Configurations of the vortex convection problem: (*top*) numerical grid; (*bottom*) overhead view of initial distribution of $-p'$. Grid lines are coarsened by a factor of 2 for visualization.

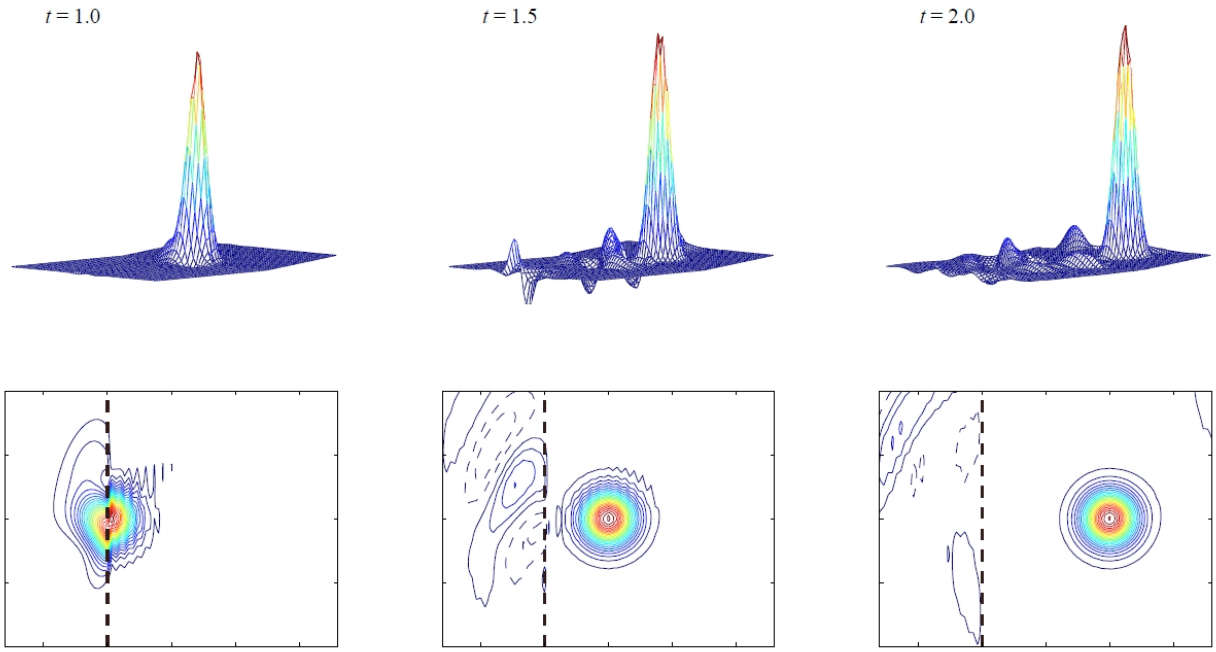

Fig. 12 Snap shots of $-p'$ distribution for the SC scheme: (*top*) overhead views; (*bottom*) contours near the interface. One contour level indicates $0.2 \times 10^{-6} p_\infty$; a dashed contour line denotes a negative value.

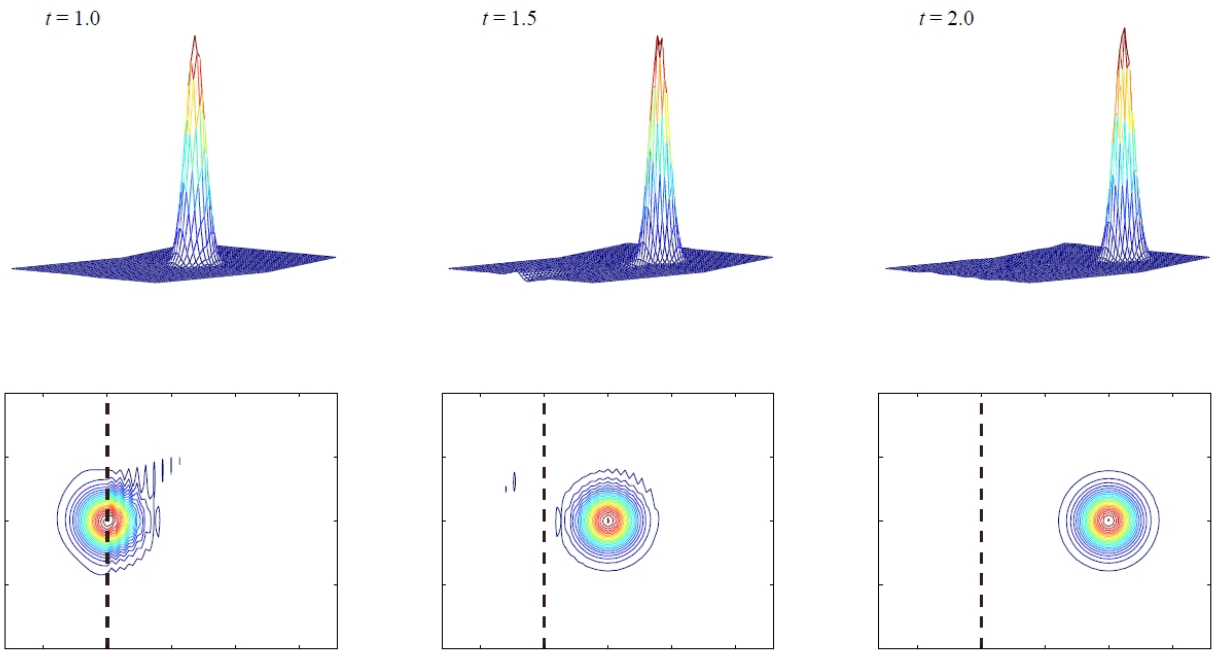

Fig. 13 Snap shots of $-p'$ distribution for the present scheme. See the caption in Fig. 12.

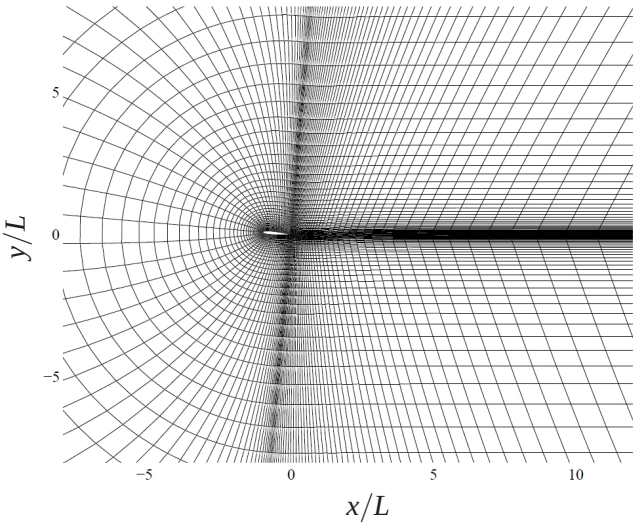

Fig. 14 C-grid topology around the airfoil. Grid lines are coarsened by a factor of 5 for visualization.

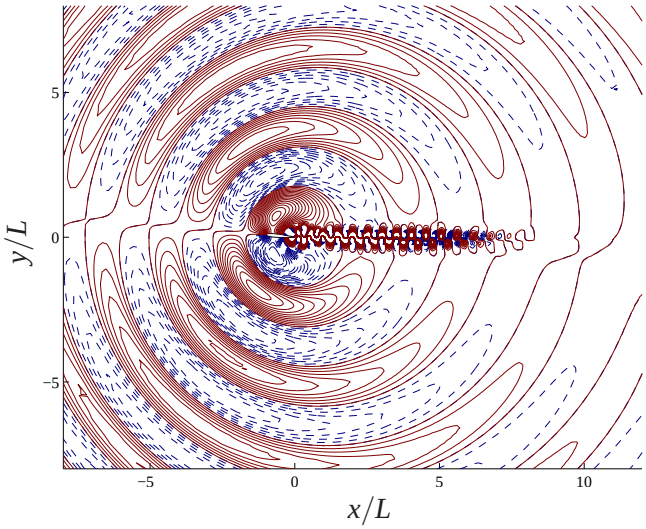

Fig. 15 Instantaneous pressure fluctuation, δp. One contour level denotes $2.0 \times 10^{-5} p_\infty$. The solid and dashed lines denote positive and negative values, respectively.

4.2 Sound generation from a 2-D airfoil

Finally, the present interface scheme is tested in an application problem of computational acoustics. In the flow past a two-dimensional object at a relatively low Reynolds number, it is well known that an aeolian tone is generated accompanied with Karman vortex shedding. Direct simulations are able to reproduce this sound generation by using high-order numerical schemes. When constructing a numerical grid, however, a great care must be taken not to affect the sound pressure that can be the order of 10^{-4} or less [3].

As a verification test of the present methodology, we simulate the sound generation from an NACA0012 airfoil using a C-grid with the interface condition applied. The flow conditions are summarized as follows: the inflow Mach number $M = 0.2$; the Reynolds number $\mathrm{Re} = U_\infty L/\nu = 5000$, where L is the chord length, ν is the kinematic viscosity at infinity; the angle of attack is 5°.

We have a reference case for this flow configuration: the numerical study by [4] also examined the noise generation from the foil using a sixth-order compact scheme. Nearly 2 million grid points were imposed on a C-grid topology to resolve the two-dimensional sound field up to $30L$ from the airfoil; a buffer layer was added to $500L$. However, they employed a Cartesian grid for the region behind the trailing edge to remove a possible adverse effect on noise generation due to curved grid lines. In addition, the derivative in the vertical direction was evaluated continuously in the Cartesian region to avoid the use of an interface connection in the wake region.

In our calculation, the numerical domain is limited to $30L$ in the radial direction, and $50L$ in the downstream region, with a non-reflecting boundary condition applied to both the boundaries. Only a near- to middle-field is of interest for a quantitative comparison of sound levels to the reference case. Therefore, the number of grid points is rather small: $900 \times 250 = 0.23$ million. We also conducted a grid-convergence study to confirm that the near-field velocity and pressure fluctuations do not greatly vary by increasing the grid resolution, although the far-field pressure level does show the adverse effects of the present coarse grid, typically for $r > 10L$. The numerical grid is shown in Fig. 14. The airfoil is tilted by 5° to the streamwise direction; the trailing edge of the airfoil is located at the origin. The interface condition is applied along with the grid line extended from the trailing edge. As seen

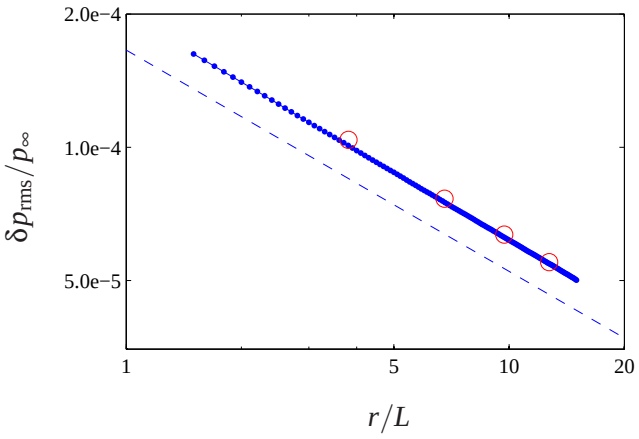

Fig. 16 Decay of pressure fluctuation: •, the present result; ◯, Irie et al. [4]. The dashed line denotes $r^{-1/2}$ dependence for reference.

from the figure, no efforts were made to smooth the grid near the interface connection. Rather, the grid holds the singular slope variation. Since the generated Karman vortices are supposed to convect along with the interface line, an ill-formed interface condition would easily create a fictitious pressure disturbance from the connection.

Fig. 15 shows the instantaneous pressure fluctuation, after the Karman vortex has fully developed in the wake region. The obtained frequency of vortex shedding is 1.8, normalized by U_∞/L, which agrees with that reported in the reference case. Generally, the pressure field is more prone to receive numerical errors, as was seen in Section 4.1. However, these pressure visualizations clearly capture the propagation of a dipole sound generated at the airfoil. No spurious pressure fluctuation is recognized at the interface connection, where the vortex street coexists. This sound pressure field is also consistent with that shown in [4].

To quantitatively examine the obtained sound pressure, the root-mean-square values of pressure fluctuation, $\delta p_{\rm rms}$, are plotted in Fig. 16, on the radial distance vertically upward from the middle of the airfoil. The amplitude of a dipole sound shows the dependence on $r^{-1/2}$ [3]; it is also shown in the figure. By comparing the present result to the reference case, although a slight discrepancy can be seen relatively near the foil, these two results agree quite well, in spite of the difference in the grid resolution. The result is presented up to $r = 15L$. Beyond that, $\delta p_{\rm rms}$ obtained in the present calculation starts to deviate from the $r^{-1/2}$ dependence due to the insufficient resolution. Nevertheless, this comparison provides an adequate validation for the present numerical treatment, in conjunction with the qualitative behavior of a dipole sound generation observed in Fig. 15.

5 Summary and conclusion

We presented an interface condition using finite-difference compact schemes suited to CAA problems. The modified wave number analysis indicates that we can reduce an anti-diffusion effect, which may be caused by the boundary closure of compact schemes, by employing the convection term evaluated on the upwind side of the interface as its boundary condition, even if centered difference stencils are used for inner nodes. By utilizing an explicit finite-difference form at boundary nodes, this requirement is satisfied naturally. We proposed a combination of standard difference forms as a model scheme, to implement the interface condition. The validity of this method was also confirmed through *a posteriori* studies in terms of both stability and accuracy.

The extension of the interface condition to a general multi-dimension case was attained through the transformation on the local grid coordinates adjacent to an interface. As a two-dimensional test case, a weak vortex convection across an interface was examined, and the obtained results demonstrate that the present implementation of the interface condition has great advantages. As a CAA application problem, the flow past a two-dimensional airfoil was simulated on a C-grid topology. In spite of the grid singularity placed in the wake region, the present scheme successfully reproduced the Karman vortex shedding, and the associated aeolian tone generation from the airfoil. The quantitative agreement with an available DNS study also supports the validity of our methodology: this approach minimizes the spurious sound generation at the interface

connection without taking a great care for mesh smoothing. This will allow the accessible use of high-order schemes to more complicated geometries, especially in three-dimensional problems.

References

[1] M. H. Carpenter, D. Gottlieb, and S. Abarbanel. The stability of numerical boundary treatments for compact high-order finite-difference schemes. *J. Comput. Phys.*, 108: 272–295, 1993.

[2] T. Imamura, S. Enomoto, Y. Yokokawa, and K. Yamamoto. Simulation of the broadband noise from a slat using zonal LES/RANS hybrid method. *AIAA-2007-226*, 2007.

[3] O. Inoue and N. Hatakeyama. Sound generation by a two-dimensional circular cylinder in a uniform flow. *J. Fluid Mech.*, 471: 285–314, 2002.

[4] T. Irie, N. Hatakeyama, and O. Inoue. Direct numerical simulation of aerodynamic noise around an airfoil. In *Proc. Eighth Japan-Russia Joint Symp. on Comput. Fluid Dyn.*, pages 14–15, Sendai, Japan, 2003.

[5] S. A. Jordan. The spatial resolution properties of composite compact finite differencing. *J. Comput. Phys.*, 221:558–576, 2007.

[6] J. W. Kim. Optimised boundary compact finite difference schemes for computational aeroacoustics. *J. Comput. Phys.*, 225:995–1019, 2007.

[7] J. W. Kim and D. J. Lee. Generalized characteristic boundary conditions for computational aeroacoustics. *AIAA J.*, 38(11):2040–2049, 2000.

[8] J. W. Kim and D. J. Lee. Characteristic interface conditions for multiblock high-order computation on singular structured grid. *AIAA J.*, 41(12):2341–2348, 2003.

[9] S. K. Lele. Compact finite difference schemes with spectral-like resolution. *J. Comput. Phys.*, 103:16–42, 1992.

[10] T. K. Sengupta, G. Ganeriwal, and S. De. Analysis of central and upwind compact schemes. *J. Comput. Phys.*, 192:677–694, 2003.

[11] J. C. Strikwerda. Initial boundary value problems for the method of lines. *J. Comput. Phys.*, 34:94–107, 1980.

[12] Jungsoo Suh, S. H. Frankel, L. Mongeau, and M. W. Plesniak. Compressible large eddy simulations of wall-bounded turbulent flows using a semi-implicit numerical scheme for low Mach number aeroacoustics. *J. Comput. Phys.*, 215:526–551, 2006.

[13] T. Sumi, T. Kurotaki, and J. Hiyama. Generalized characteristic interface conditions for accurate multi-block computation. *AIAA-2006-1217*, 2006.

[14] M. R. Visbal and D. V. Gaitonde. Padé-type higher-order boundary filters for the Navier-Stokes equations. *AIAA J.*, 38:2103–2112, 2000.

[15] M. R. Visbal and D. V. Gaitonde. On the use of higher-order finite-difference schemes on curvilinear and deforming meshes. *J. Comput. Phys.*, 181:155–185, 2002.

Copyright Statement